JOURNAL OF MATERIALS SCIENCE 35 (2000) 3817–3826

High-brightness laser welding of thin-sheet 316 stainless steel

M. FARID, P. A. MOLIAN
Mechanical Engineering Department, Iowa State University, Ames, IA 50011, USA
E-mail: molian@iastate.edu

Photolytic iodine laser (PIL), a new industrial laser in the market, offers much higher brightness than existing Nd:YAG and CO_2 lasers. PIL has also a unique wavelength (1315 nm) that has not yet been tested for welding applications. In this work, the capabilities of PIL for precision seam welding of 0.1-mm thick sheet of AISI 316 stainless steel in the lap-joint configuration were evaluated. The weld performance data of PIL laser were compared with Nd:YAG and CO_2 lasers. The astounding benefits of PIL weld are narrow seam, extremely fine solidification cell structure, fully austenitic microstructure, and small heat-affected-zone (HAZ). These benefits are attributed to the PIL's high brightness that in turn enables achieving small spot size and energy transport through plasma rather than by heat conduction. In contrast, the welds produced by Nd:YAG and CO_2 lasers exhibited wider seams, coarser solidification structures, duplex microstructures of austenite and ferrite, and larger HAZ due to slow cooling of the melt, and lateral heat diffusion. Despite the narrow seam, the PIL weld carried a high tensile load (92% that of base metal) and was harder than the base metal. Microstructural analysis revealed that PIL welds exhibited fully austenitic structures and were free from hot cracking. These advantages are consequences of the rapid solidification effects including large undercooling, minimal segregation of impurities to the grain boundaries, and fine grain size.

1. Introduction

There exists a demand for a high quality, faster joining method to spot and seam weld thin-sheets (<0.2 mm) of similar and dissimilar metals including stainless steels, galvanized steels, aluminum alloys, and copper alloys. The applications include electronic components, medical instruments, thin tubes, actuators, metal gaskets, pumps, tanks, etc. The direct impact on sheet-metal industry will be reduced production costs, higher production rates and flexibility in the size. The industry seeks the following properties in thin-sheet metal welds: strength equal or greater than that of base metal; small weld size; continuous seam; and absence of defects and distortion.

A review of literature indicates [1] that the most appropriate processes for joining thin-sheet metals in butt and lap joint configurations are tungsten-inert-gas (TIG) arc, plasma (PA), resistance seam (RSE), laser beam (LBW), cold-pressure (CPW), brazing (B) and adhesive bonding (AB). TIG, PA and RSE welding processes were excluded for sheets less than 0.1 mm thick because these processes do not provide the heat input in a controlled form. B and AB methods do not result in the strength required in the joint and may be omitted from further consideration. LBW and CPW are two processes that would work well for thin-sheets. CPW requires a substantial amount of tooling, post-trimming, and needs metals with good ductility. This leaves LBW as a viable option to meet the stringent performance requirements of the industry.

In today's laser manufacturing applications market, laser welding has about 35% share, the second largest segment of the market. In general, laser welding has experienced slow acceptance by the manufacturing community because parts were designed to accommodate conventional welding techniques. In laser welding, a focused laser beam is used to produce a melt puddle that is protected by a shroud of low-velocity inert gas such as helium or argon. The melt is then used to join the two parts. Although parts with a thickness of up to 50 mm have been welded in single pass, most laser welding is confined to parts with a thickness of 7.6 mm or less. Laser welding is most widely known for its deep penetration capability, although it can be successfully used in the conduction-mode for thin-sheet metal welding. It has been demonstrated [2] that a pulsed Nd:YAG laser is currently the best source for welding metals such as aluminum, stainless steel, tantalum, and nickel with thickness less than 0.125 mm. However, the common problems associated with CO_2 and Nd:YAG laser welding of thin-sheet metals are wider welds with melt-through, loss of material by evaporation, contamination, porosity, humping, seam discontinuity, seam narrowing, pronounced concavity/convexity of the weld seam, inclusions, pinholes, cracking, distortion, residual stresses, incomplete weld, undercut, and poor bead appearance [3–11]. Recent technological developments in photonics led to advanced lasers including PIL, fiber laser, and diode-pumped solid-state laser. The benefits of higher brightness, compactness, and efficiency made

these advanced lasers ideal candidates for precision materials processing.

PIL, a new industrial laser with powers up to 100 W, was made available by Advanced Optical Equipment and Systems Corporation (AOESC) [12]. A microwave-pumped, closed-cycle gas laser, PIL uses the inert refrigerant C_3F_7I. It possesses superior beam quality and excellent repeatability. The beam can be focused down to a spot size of 7 μm with no loss of power. AOESC estimates that PIL will perform five times better than the fast axial flow CO_2 laser, and 12.5 times better than the face-pumped slab Nd:YAG laser per unit cost [12]. The operating cost of PIL would be same as that of CO_2. It is projected that a 150-W PIL laser can outperform 15 times a 1000-W CO_2 and 11 times a 500-W Nd:YAG [12].

The brightness, the most significant benefit offered by PIL over the existing industrial lasers, is 30 times higher than rod-type Nd:YAG laser [12]. While the intensity can be varied, the brightness of a laser source remains invariant. The brightness of a laser source is defined as the power emitted per unit surface area per unit solid angle per unit bandwidth. The brightness can be expressed as:

$$B = \frac{P}{\Omega A(\Delta\lambda)} \tag{1}$$

where $P =$ laser power, $\Omega =$ solid angle $= \pi\theta^2/4$, $\theta =$ angle of divergence, $A =$ spot area, and $\Delta\lambda =$ bandwidth. In addition to brightness, PIL produces longer waist at the focal region that minimizes the inconsistency and/or drifting performance usually encountered in welding with existing lasers. For example, the rod-type Nd:YAG lasers are capable of producing good quality welds but have a repeatability of less than 50%. PIL also provides a wavelength of 1315 nm that is unique to welding.

2. Experimental methods and materials

The material used was AISI 316 stainless steel (Cr 16-18, Ni 12-14, Mo 2-3, C 0.08, Fe balance) in the form of 0.1-mm thick sheets. AISI 316 steel is well known for its excellent corrosion and creep resistance. The rationale for choosing this steel is that it is used in the welded form for numerous applications. The annealed stainless steel sheets, received in the form of 300 mm square, were sheared to a size of 150 mm $\times$ 50 mm suitable for sample welding. Excessive curling of the edge and sharp burrs were eliminated by using a metal ruler over the surface of the strips. Three continuous wave (CW) lasers, CO_2, Nd:YAG and PIL (Table I), were used for seam welding.

The experimental set-up consists of laser, welding fixture, positioning table with a computer numerical controller, and assist gas system. In this work, only lap-joint configuration was considered because butt joints are difficult to produce in 0.1-mm thin sheets. Fig. 1 shows the welding fixture that ensures accurate positioning, prevents the movement of the part due to thermal distortion, and acts as a good heat sink. The fixture assembly consisted of a laboratory jack, a fixture plate,

TABLE I Specifications of the lasers used in this work

Characteristic	PIL-CW	Nd:YAG-CW	CO_2-CW
Wavelength, nm	1315	1064	10,600
Spot size, mm	0.02	0.4	0.25
M^2	1.1	100	3.0
Laser Power, W	10–20	10–20	200–600

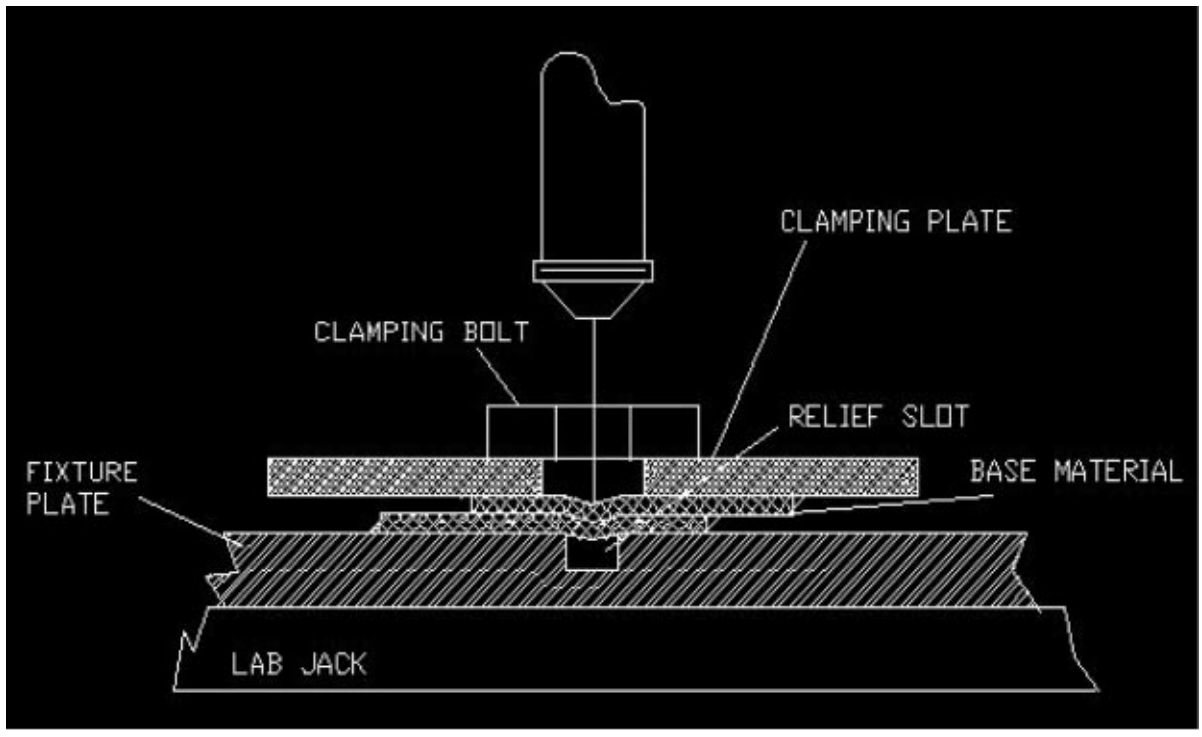

Figure 1 Schematic of the laser-welding fixture used in experiments.

one clamping bar and two clamping bolts. The laboratory jack allowed for the vertical adjusting of the standoff height. The aluminum fixture plates provided a flat work surface to clamp the samples. The fixture plate had a relief slot with dimensions 125 mm × 3 mm × 3 mm machined onto its surface. The purpose of slot was to prevent the joining of sample to the fixture plate. The clamping bar had a slot of the same dimensions machined through it. The samples were firmly clamped to each other (without any air gap) and to the fixture plate because the air-gap in the lap joint can substantially reduce weld penetration and lead to the formation of porosity. Compressive clamping through proper fixture design and 'creasing' (deforming) of the overlap region was carried out to obtain good lap joints.

A 127-mm focal length lens was used to focus the laser beam. The beam was passed through a nozzle diameter of 4 mm. The standoff distance between the nozzle and the metal was between 20 mm and 25 mm. Argon was flown as an assist gas at a flow rate of 0.4 to 0.5 liter/sec (50 to 70 cfh) during welding. Although helium is usually recommended as an assist gas to eliminate the plasma that forms during laser welding, it did not work well in our experiments. In fact, it was mysterious to observe that the welds could not be made when helium was used as the assist gas.

Both destructive and nondestructive tests were carried out to evaluate the weld joints. Tensile testing of samples with dimensions of 50-mm long and 25-mm wide was conducted in an electromechanical tensile machine (MTS system with a capacity of 100,000 N) at a strain rate of 0.1 mm/sec. The maximum load that the specimen could support was measured. Hardness tests were carried out in a Tukon micro hardness tester at a load of 50 gmf using a Vicker's diamond pyramid indenter. For hardness testing, the weld sample was cut into 8 mm × 8 mm squares and then mounted on Bakelite. These samples were then polished and etched prior to conducting the hardness tests. Micro X-ray nondestructive evaluation (NDE) testing was used to evaluate the continuity, uniformity and defects of the welds. The micro X-ray imaging system consisted of micro X-ray source, video camera, data processing system, and five-axis CNC table for mounting the samples. There were two identical images produced as a result of data processing. One image is nothing but the negative of the other. These images defined the uniformity of the weld and provided information on the defects.

Microstructural characterization was carried out by optical microscopy, scanning electron microscopy, and X-ray diffraction (XRD) using CuK_α radiation. Standard metallographic procedure was employed to prepare the specimens for optical microscopy. The specimens were etched with a mixture of acids. A JEOL JSM 35 scanning electron microscope with an energy dispersive spectrometer (EDS) was used to characterize the longitudinal and transverse sections of the weld for flaws and solidification structure. The concentration profiles of Cr, Ni, and Mo in the fusion zone were analyzed to determine the microsegregation. The ferrite content of microstructure was evaluated magnetically using a device called Magnescope and was confirmed with XRD data.

TABLE II Laser parameters and property data of PIL welds

Sample	Process Parameters, Power, speed, gas	Weld width, μm	HAZ, μm	Vicker's Hardness	Tensile Strength, MPa
Weld # 1	20 W, 0.55 m/s, Ar	240–250	50	167	550–570
Weld # 2	20 W, 3.1 mm/s, Ar/O_2	250–260	50	200	440–480
Base Metal	—	—	—	122	600–630

3. Experimental results

3.1. PIL laser welding

The laser power was varied from 10 to 20 W. Five batches, each containing five to seven samples, were produced for each power setting. Analysis of the full-penetration welds revealed that the welding speed varied linearly with laser power according to $V = 0.3P$ where $V =$ welding speed, mm/sec, and $P =$ laser power, W. Table II lists the laser parameters and properties of two representative, full-penetration welds. The welds exhibited a width close to spot size and small HAZ. In order to increase the welding speed, a small amount of oxygen was added to the argon assist gas during welding. Oxygen enhanced welding speed, increased the hardness, eliminated the discontinuity of the weld and subsequently improved the bead appearance. However, the tensile test results indicated that oxygen reduced the load carrying capacity of weld by forming oxide inclusions.

Fig. 2 is a scanning electron micrograph of the transverse section of Weld # 1 showing the flaw-free weld zone. Fig. 3 is an optical micrograph of the longitudinal seam of Weld #1 showing the presence of highly disturbed, "unstable" melt during welding. The melt pool instability is due to the turbulent flow conditions caused by the small diameter and high-temperatures of molten pool. Micro X-ray NDE images of the welds, shown in Fig. 4, characterize the discontinuities and show that addition of a small amount of oxygen to argon during welding improved the continuity of weld bead by eliminating the turbulence conditions. The hardness and tensile load of the weld were decreased with an increase in the number of discontinuities as determined by the micro X-ray images.

3.2. Nd:YAG laser welding

Welding was conducted with the same laser parameters as those of PIL except, of course, the brightness. Although the brightness was much lower for YAG compared to PIL, higher welding speeds were achieved because plasma was not a serious problem. However, the weld sizes (fusion zone and HAZ were 750 μm–1000 μm and 200–250 μm respectively) were three to four times larger than PIL welds. Figs 5 and 6 are the transverse section and the longitudinal seam respectively. The micro X-ray NDE image (Fig. 7) confirmed that the weld was continuous and uniform. Tensile tests of the welds indicated that the tensile strength was 530–550 MPa. The hardness was 150 HV on the average.

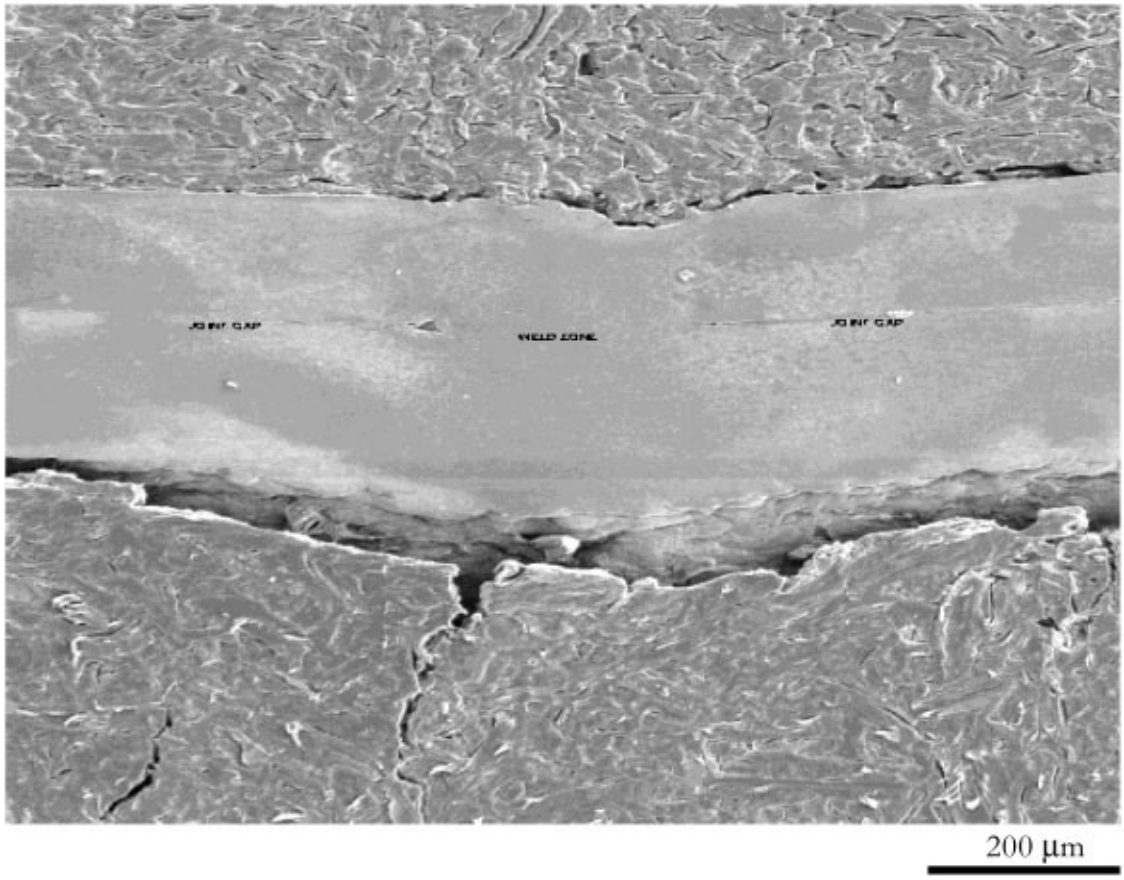

Figure 2 Transverse section of Weld #1.

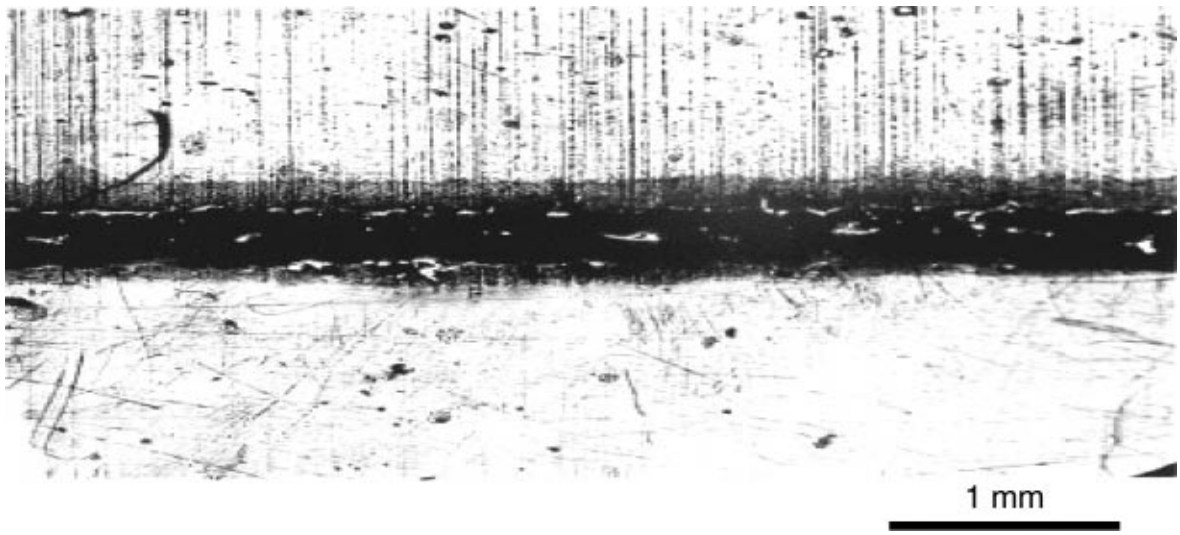

Figure 3 Optical micrograph showing the longitudinal seam of Weld #1.

3.3. CO_2 laser welding

CO_2 laser welding required higher power (>200 W) due to increased reflectivity of the metal surface and energy loss in the plasma. The higher the power, the higher the speed at which the welding could be carried out. Table III provides the weld parameters and property data. The weld width and HAZ were intermediate of those of PIL and YAG welds. The tensile load carrying capacity of the weld increased with an increase in laser power. Visual examination showed that the welds were free from cracks and porosity but had some contamination. Figs 8 and 9 show the transverse section

TABLE III Laser parameters and property data of CO_2 laser welds

Sample	Process Parameters, Power, speed, gas	Weld width, μm	HAZ, μm	Vicker's Hardness	Tensile Strength, MPa
3	200 W, 21 mm/s, Ar	470	140	185	450–460
4	400 W, 53 mm/s, Ar	460	140	190	480–500
5	600 W, 95 mm/s, Ar	460	140	180	510–530

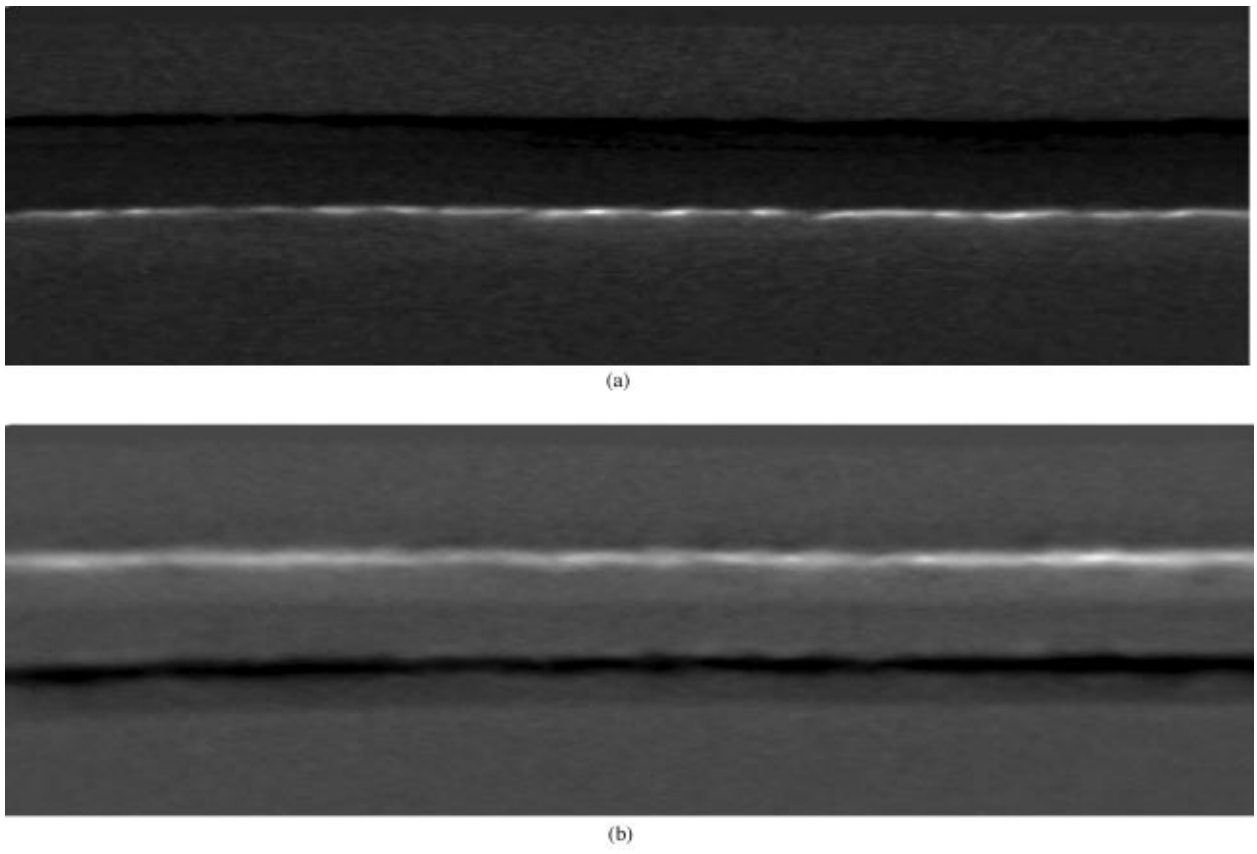

Figure 4 Micro X-ray NDE images of (a) Weld #1 and (b) Weld #2.

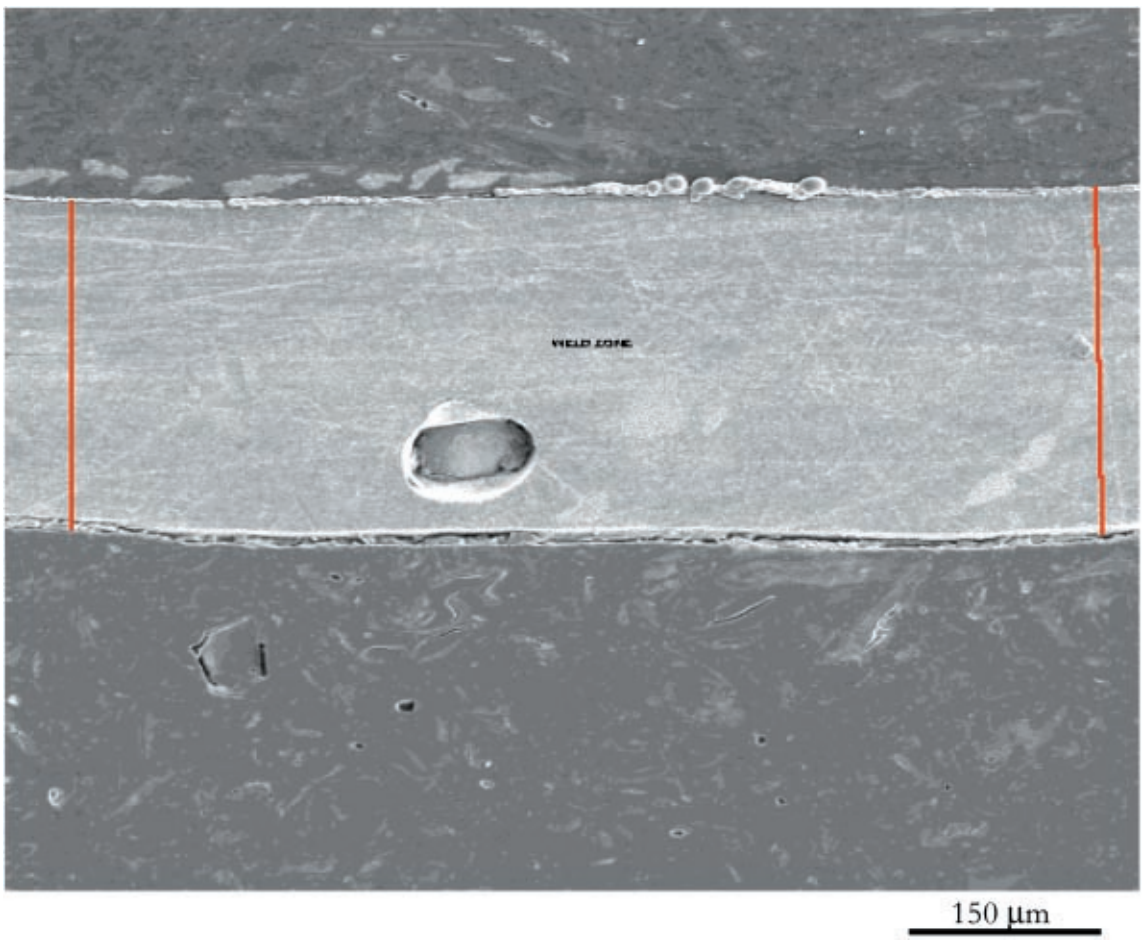

Figure 5 Transverse section of the YAG weld. Note the presence of a large pore.

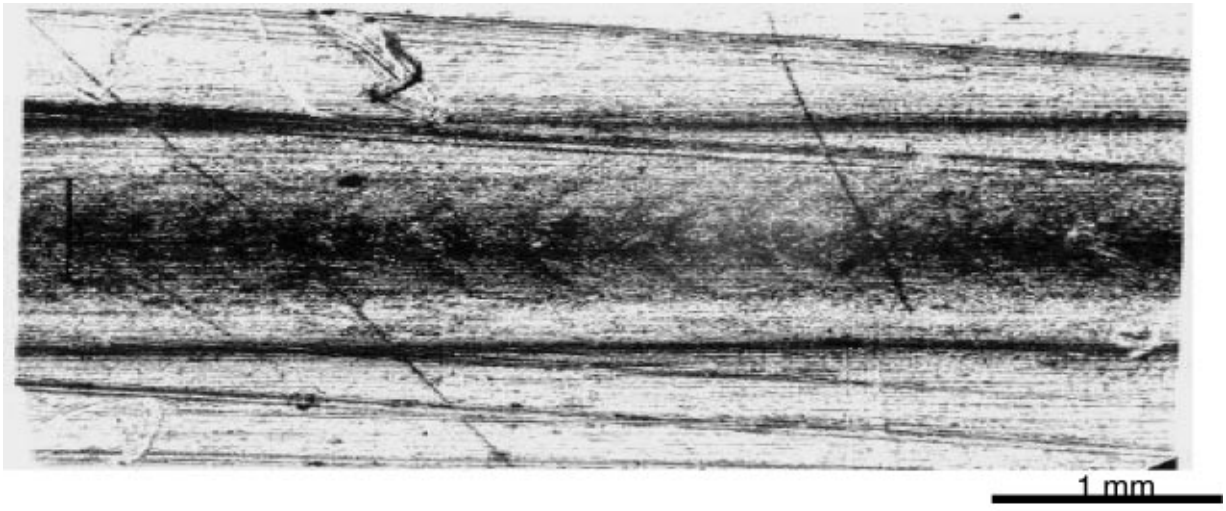

Figure 6 Optical micrograph of the longitudinal seam of YAG weld.

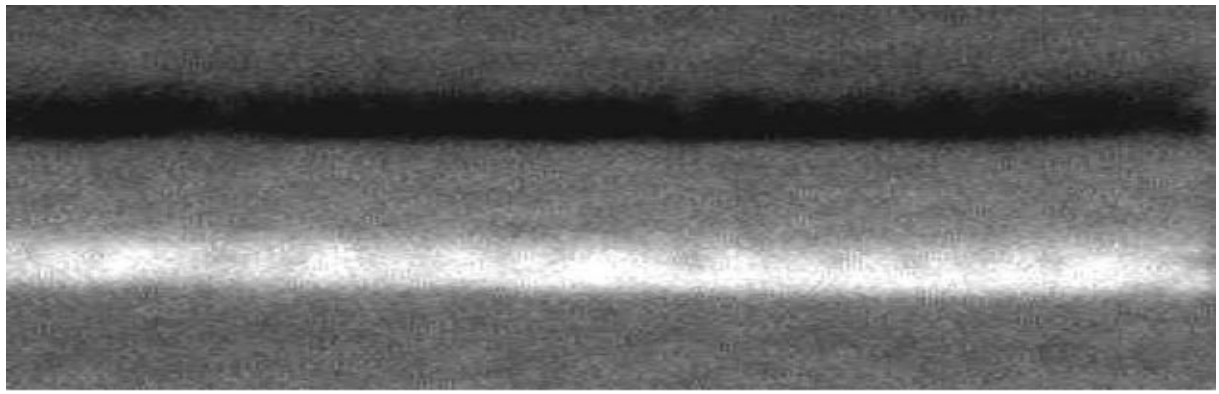

Figure 7 Micro X-ray NDE image of YAG weld.

and longitudinal seam of the weld. Micro X-ray NDE images (Fig. 10) revealed that the welds produced at low power were discontinuous and, consequently, had lower strengths.

4. Discussion

4.1. Energy balance

The conduction-limited laser welding with high-brightness laser (PIL) is quite different from those of low-brightness lasers. The energy-coupling problem is sharply reduced with PIL laser although the initial reflectivity as a function of wavelength (Drude's free electron model) remains more or less same as YAG. In welding, the laser energy absorbed by the metal is dissipated in three ways. First, the energy is converted into heat used for melting the metal to form the fusion zone. The conduction of heat away from the melting front in solid state is usually obtained by solving three-dimensional classical heat conduction equation. Second, the convection of melt pool through surface deformation and thermocapillary effects are generally obtained by solving time-dependent, incompressible Navier-Stokes equations and pressure balance equations. Third, the plasma absorbs, reflects, or transmits laser energy depending on the relationship between the frequency of plasma and the frequency of laser beam. From most of the investigations of metal welding with lasers, it is found that the beam can transmit through the plasma. However, the plasma is not a perfect transparent medium and absorbs a portion of the incident energy by the Inverse Bremsstrahlung (photon-electron interaction) effect. Plasma physics theory can be used to calculate the amount of laser energy absorbed by the plasma if the electron density, plasma temperature and frequency are known [13]. The measurements of plasma properties are indeed complex.

In this work, a simple energy-balance approach was used to estimate the energy losses associated with laser welding. The overall energy balance is represented by:

$$E_1 = E_2 + E_3 + E_4$$

Where $E_1 =$ absorbed laser energy input, $E_2 =$ energy required for the weld with a width equal to spot size, $E_3 =$ energy loss by heat conduction to form the "wasted" melt and HAZ, and $E_4 =$ energy loss through plasma. Experimental data were used to fit the above equation and to estimate the energy loss through plasma. Table IV summarizes thermodynamic energy data of the welds produced by different lasers. It is evident that PIL welding is accompanied by a greater energy transport through plasma rather than by heat conduction.

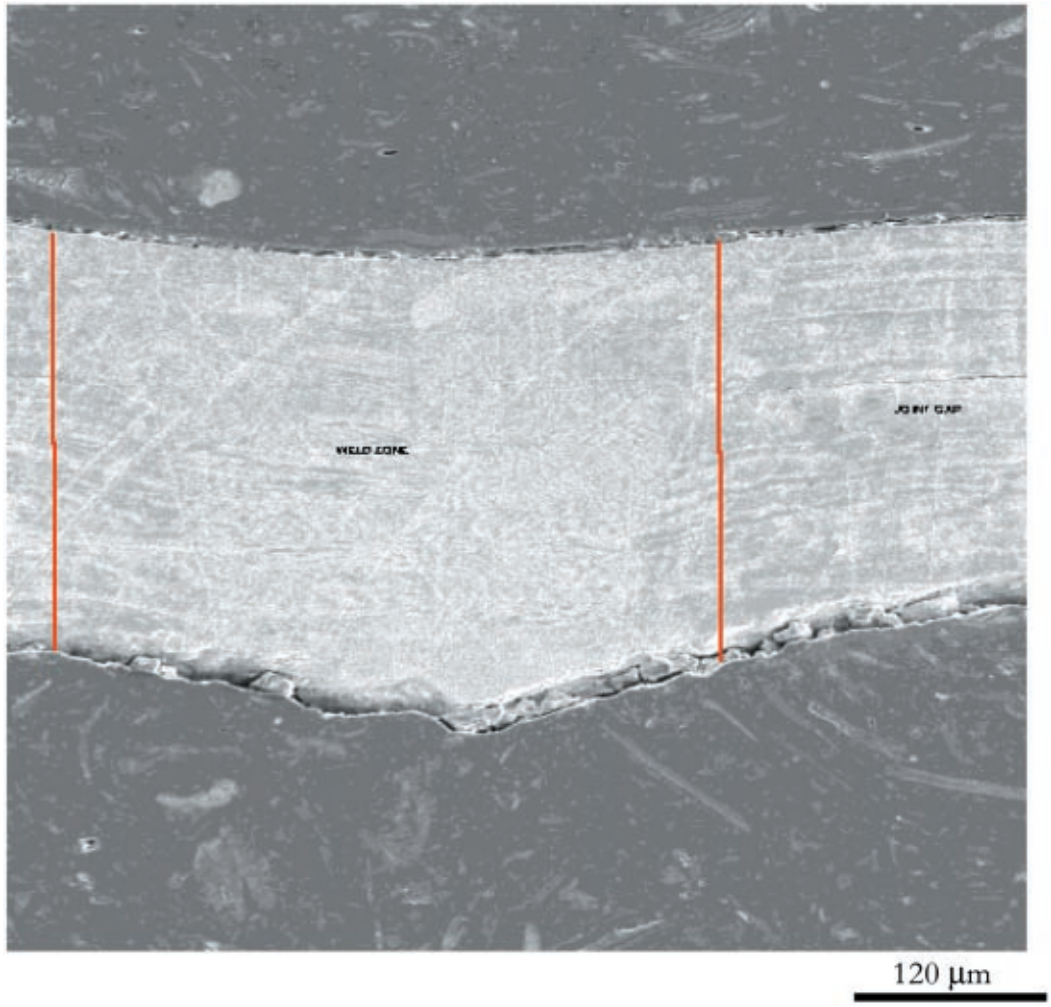

Figure 8 Transverse section of the CO_2 laser weld.

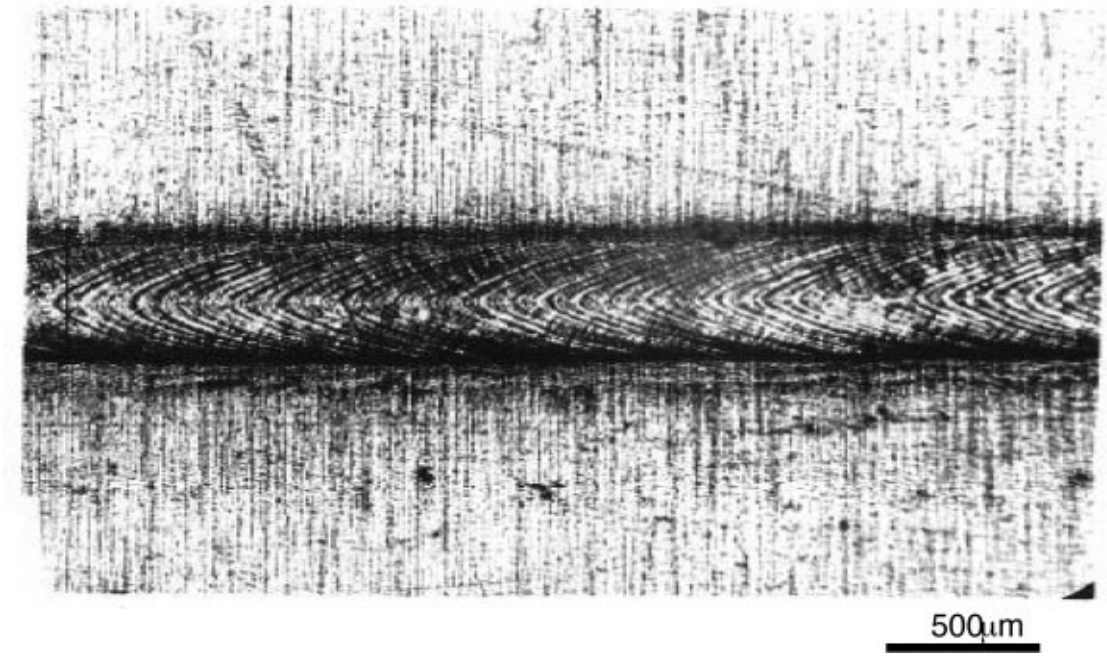

Figure 9 Longitudinal seam of CO_2 laser weld.

4.2. Microstructure and properties

The mechanical properties of welds, summarized in Table V, show that PIL has a capability to produce high strength welds. Three factors have contributed to the improvement in strength and hardness of PIL welds: fine cell structure associated with rapid solidification, small HAZ, and phases present in the microstructure. Fig. 11a to c are representative scanning electron

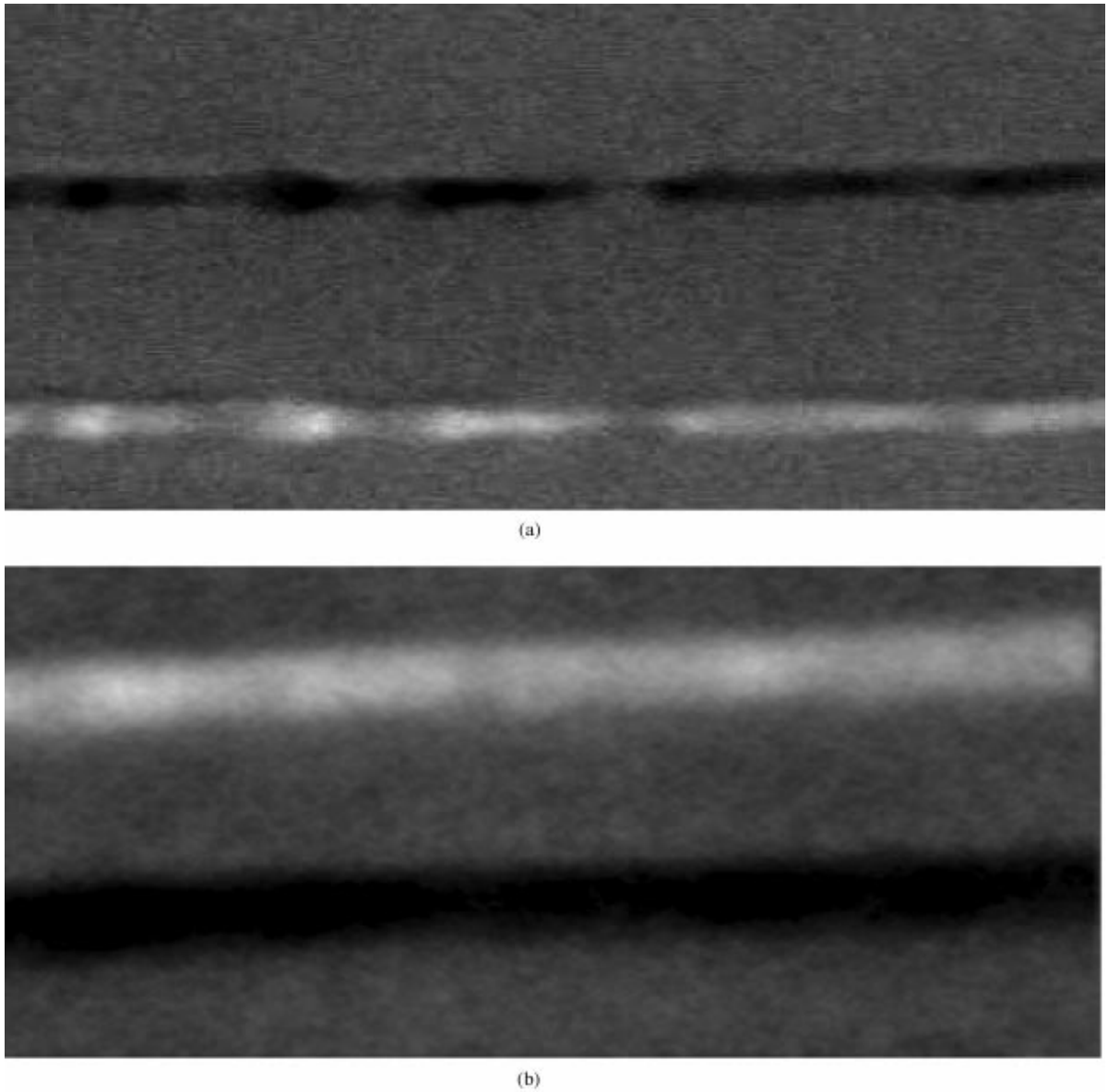

Figure 10 Micro X-ray NDE images of CO_2 laser welds (a) Sample #3 (b) Sample #5.

TABLE IV Energy balance predictions

Energy Output	PIL	Nd:YAG	CO_2
E_2-Weld	22%	10%	8%
E_3-Conduction	37%	79%	65%
E_4-Plasma	41%	11%	27%

TABLE V Summary of experimental results

Characteristic	Base Metal	PIL Weld	Nd:YAG Weld	CO_2 Weld
Weld Width, μm	—	250	750	450
HAZ, μm	—	50	200	130
Hardness, HV	120	200	150	180
Tensile Strength, MPa	620	560	540	530
Solidification Cell Size, μm	—	0.05	4	0.6
Microstructure of weld	$\gamma + \delta$	γ	$\gamma + \delta$	$\gamma + \delta$
Hot cracking	—	None	None	None

micrographs showing the cellular-dendrite structures of all laser welds. These structures were uniform throughout the weld regions and are indicative of high G/R ratios (G = temperature gradient, R = growth rate) associated with rapid solidification. The fusion zone of PIL weld exhibits extremely fine structures that are almost not discernible (Fig. 11a). In contrast, the fusion zone of YAG weld consists of coarse dendrite structures. The size of HAZ also influences the mechanical properties. PIL weld contained the smallest HAZ that in turn prevented the deleterious effects of coarse grain size and residual stresses on the mechanical properties.

Microstructural investigations showed that PIL weld consisted of fully austenite (γ), whereas YAG and CO_2 welds contained a duplex microstructure of austenite (γ) and ferrite (δ). The ferrite content was 3–4%. The EDS compositional analysis of the interdendritic and intradendritic regions revealed that the composition was essentially constant, suggesting the absence of microsegregation. Further, there was no evidence of any hot cracking in all the weldments. The microstructural

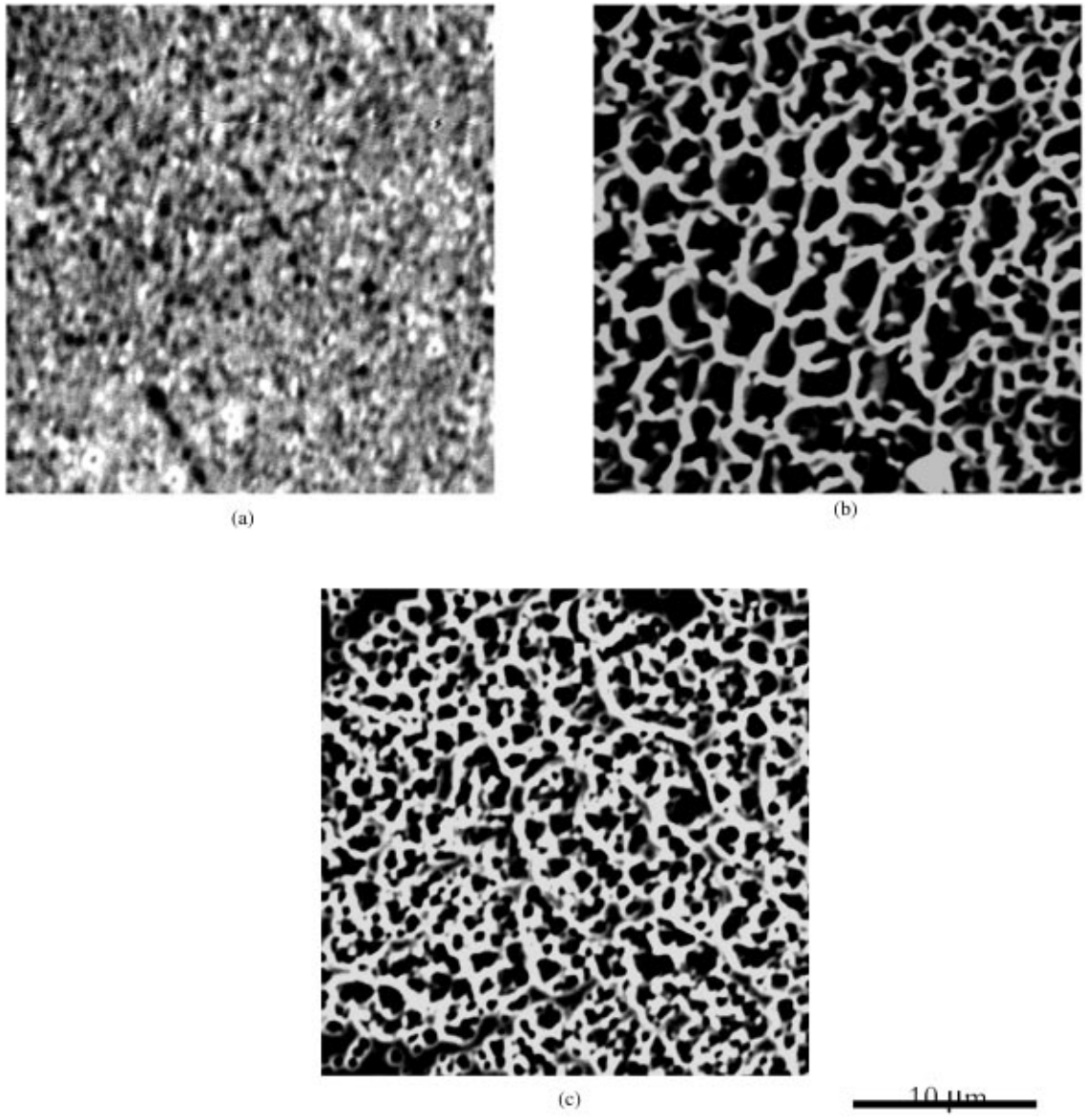

Figure 11 Solidification structures of laser welds (a) PIL (b) Nd:YAG, and (c) CO_2.

features, microsegregation aspects, and their effects on hot cracking are commonly explained based on equilibrium phase transformations.

The chromium and nickel equivalents that determine phase transformations in austenitic stainless steels are given by:

$$Cr_{eq} = \%Cr + \%Mo + 1.5\,(\%Si)$$
$$Ni_{eq} = \%Ni + 30(\%C) + 0.5\,(\%Mn)$$

For 316 stainless steel used in this work, the ratio of Cr_{eq}/Ni_{eq} is 1.33. The final microstructure, according to Schaeffler diagram, consists of austenite with less than 5% ferrite. Takalo *et al.* [14] suggested that for this Cr_{eq}/Ni_{eq} ratio, solidification will take place by primary austenite formation. Ferrite is then formed by a eutectic reaction. The pseudo vertical section of Fe-Cr-Ni phase diagram indicates that the equilibrium transformation for 316 stainless steel is:

$$\text{Liquid} \rightarrow \text{Liquid} + \gamma \rightarrow \text{Liquid} + \gamma + \delta \rightarrow \gamma + \delta$$

The amount of ferrite formed in the microstructure is sensitive to small changes in the cooling rates. A fully austenitic structure was developed in PIL weld because of the extreme cooling rates that suppressed the eutectic reaction, which allows ferrite to form. It is believed that faster cooling rates generated a large undercooling that inhibited the ferrite to form. This finding is consistent with a previous study on 304 stainless steel [15]. The presence of ferrite in YAG and CO_2 laser welds suggests that the eutectic reaction is continued probably due to moderate solidification conditions.

A major issue in welding of austenitic stainless steels is hot cracking. Coarse grain size, segregation of impurities to the grain boundaries, and long-freezing range of the alloy cause hot cracking. Under typical welding conditions, ferrite forms and protects the weld from undergoing hot cracking. The ability of ferrite to reduce hot cracking is attributed to the prevention of segregation of low-melting constituents such as sulfur and phosphorus to the interdendritic areas. However, ferrite drastically reduces the corrosion resistance and promotes high-temperature embrittlement. It is therefore desirable to produce fully austenitic structures without hot cracking for which PIL welding would be an excellent choice. PIL welds do not suffer from hot cracking

despite the absence of ferrite because the rapid solidification minimized segregation of impurities and produced fine grain size.

5. Conclusion

Photolytic iodine laser (PIL) was evaluated for capabilities to weld 0.1-mm thick sheets of AISI 316 stainless steel in lap-joint configuration. A comparison of the performance of PIL laser was made with CO_2 and Nd:YAG lasers. The PIL laser beam, focused to a spot size of nearly 0.02 mm, was efficient in producing narrow-seam welds that exhibited fine solidification cell structures, fully austenitic microstructure, and high hardness.

Acknowledgements

The authors would like to thank Metal Tech Industries, Inc., US Air Force's Phillips Laboratory, and Center for Non-destructive Evaluation at Iowa State University for support of this work.

References

1. P. HOULDCRAFT, "Which Process?" (Abington Publishing, Cambridge, UK, 1990).
2. A. C. LINGENFELTER, in Proceedings of Laser Advanced Materials Processing (High-Temperature Society of Japan, 1987) p. 211.
3. A. V. LA ROCCA, "Proceedings of Society of Photo Instrumentation Engineers, Vol. 2097: Laser Applications" (Optical Society of America, 1993) p. 100.
4. C. M. BANAS, in "Industrial Laser Annual Handbook," edited by D. Belforte (Laser Focus World, Tulsa, OK, 1989).
5. T. ZUYAO, C. CHU and D. BINGYOU, in Proceedings of Laser Advanced Materials Processing (High-Temperature Society of Japan, 1987) p. 217.
6. N. ARAI, K. OKITA, M. ARITOSHI and W. KISHIMOTO, in Proceedings of Laser Advanced Materials Processing (High-Temperature Society of Japan, 1987) p. 221.
7. J. EGGERSGLUB, G. KROHNERT and J. DRAUBE, *Proceedings of SPIE* **1022** (1988) 38.
8. R. VILAR and R. M. MIRANDA, *Proceedings of SPIE* **952** (1988) 719.
9. J. M. SIGNAMARCHEIX and M. BOUSSEAU, in Proceedings of Laser Advanced Materials Processing (High-Temperature Society of Japan, 1987) p. 205.
10. Z. LI, Z. CHEN, J. XIONG, Z. DAI and X. HU, *ibid.* p. 487.
11. Z. TANG, B. DAI, C. FENG and F. LI, *ibid.* p. 559.
12. P. R. CUNNINGHAM, Advanced Optimal Equipment and Systems Corp., P.O. Box 339, Edgewood, New Mexico 57015, private communication.
13. R. FABBRO, in Proceedings of Laser Advanced Materials Processing (High-Temperature Society of Japan, 1992) p. 305.
14. T. TAKALO, N. SUUTALA and T. MOISIO, *Metallurgical Transactions* **10A** (1979) 1173.
15. P. A. MOLIAN, *Journal of Materials Science Letters* **4** (1985) 281.

Received 2 July
and accepted 15 December 1999